Materials Research Express

PAPER • OPEN ACCESS

Investigation of the influence of process parameters on crack formation and mechanisms in Ti-48Al-2Cr-2Nb alloy via laser directed energy deposition

To cite this article: Baolei Cui *et al* 2023 *Mater. Res. Express* **10** 126509

IOP Publishing Mater. Res. Express 10 (2023) 126509 https://doi.org/10.1088/2053-1591/ad14c3

Materials Research Express

CrossMark

OPEN ACCESS

RECEIVED
25 September 2023

REVISED
30 November 2023

ACCEPTED FOR PUBLICATION
12 December 2023

PUBLISHED
21 December 2023

PAPER

Investigation of the influence of process parameters on crack formation and mechanisms in Ti-48Al-2Cr-2Nb alloy via laser directed energy deposition

Baolei Cui[1,2], **Weijun Liu**[1], **Hongyou Bian**[1], **KeQiang Chen**[1] **and Xiaowen Xu**[1]

[1] School of Mechanical Engineering, Shenyang University of Technology, Shenyang, Liaoning, People's Republic of China
[2] School of Mechanical and Electrical Engineering, Shenyang Aerospace University, Shenyang, Liaoning, People's Republic of China

E-mail: cuibaolei201900013@smail.sut.edu.cn

Keywords: Ti-48Al-2Cr-2Nb Alloy, laser directed energy deposition, mechanism of crack formation, laser remelting

Abstract

The Ti-48Al-2Cr-2Nb alloy was fabricated using laser directed energy deposition(LDED), and the impact of various process parameters on the macroscopic crack morphology was analyzed. The mechanism of crack formation was investigated through the analysis of crack microstructure, phase composition, crystal orientation, and elemental composition. The process parameters were optimized by response surface methodology(RSM) and the laser remelting method was used to suppress the crack formation. The results showed that the cracks were mainly caused by lack of fusion, residual stress during LDED and stress between different phases of TiAl alloy. The mismatch of process parameters results in insufficient energy for powder melting, ultimately leading to lack of fusion occurrence. To minimize crack formation, the response surface method was employed to optimize process parameters and reduce crack generation. The higher temperature gradient led to the existence of residual stress in the sample, and the higher stress between α_2 phase and B_2 phase formed in the deposition process due to the difference of thermal expansion coefficients. The region where the two phases converge was the region with the highest crack sensitivity, and cracks occured in the region where α_2 phase and B_2 phase converge in the form of excellent transgranular fracture. The samples prepared by using the optimized parameters can effectively restrain the cracks caused by lack of fusion, but can not restrain the cracks caused by the stress between phases. Laser remelting after LDED can not only reduce the temperature gradient and residual stress, but also remelt the unmelted powder on the surface of the as-deposited samples, effectively inhibiting the generation of cracks, and preparing crack-free samples.

1. Introduction

TiAl alloy is considered to be a potential high temperature structural material for supersonic spacecraft, future gas turbine engine, high speed civil transport aircraft and so on because of its low density, high elastic modulus, high specific strength, excellent corrosion and oxidation resistance and flame retardancy at high temperature, high fatigue strength and creep strength [1, 2]. In the development of advanced materials, TiAl alloy has become the preferred structural material to replace the nickel-based superalloy for low pressure turbine (LPT) blades of gas engines, which is expected to reduce the structural weight of low pressure turbine (LPT) blades of high performance engines by 20%~30% [3]. Additive manufacturing technology is an advanced rapid near net forming technology developed rapidly in 1990s. In contrast to conventional manufacturing techniques, such as equivalent manufacturing (casting, forging, and soldering), and subtractive manufacturing (milling, turning, and grinding), additive manufacturing is particularly suitable for single-piece prototyping and rapid production of intricate components that are challenging or even impossible to manufacture using traditional methods. Leveraging this advantage, additive manufacturing is increasingly employed for the rapid development of intricate structural products and equipment, thereby enabling significant time and cost efficiencies [4–8]. The synchronous powder feeding characteristic of laser directed energy deposition(LDED) enables the manufacturing of TiAl-based alloy coatings for surface modification of parts. Furthermore, the utilization of a multi-channel powder feeding device allows for the preparation of functional gradient materials and composites based on TiAl, facilitating the integrated manufacturing of parts with multiple materials and structures [9, 10], such as double alloy integral blade discs and impellers [11, 12]. The LDED equipment exhibits excellent versatility, as it allows for the incorporation of synchronous heat sources (such as resistance, induction heating devices, and secondary laser sources), thereby enabling effective elimination of internal stress and controlled prevention of forming cracks. During the LDED process, the high-energy laser beam induces a significant temperature gradient and cooling rate, leading to stress generation. With the gradual accumulation of these stresses, it becomes prone to the formation of cracks and other defects [13–15]. Especially for TiAl alloy with poor plastic deformation ability and low room temperature ductility, cracks are more likely to occur [16–18]. Because the phase composition of TiAl alloy includes γ, α_2 and β, and the intense and complex reaction occurs in the LDED process, it is necessary to further study the mechanism and suppression methods of cracking in TiAl alloy by LDED. Liu [19] reduced the tendency of crack formation by increasing laser energy input, but it could not completely eliminate cracks. It was found that preheating the substrate of TiAl alloy prepared by LDED can reduce the tendency of crack formation [20]. Sharman [21] and Thomas [22] found that under the condition of appropriate laser power, the powder was preheated by rotating the objective, adjusting the focus position to increase the laser spot size, and the cooling rate of molten pool decreased, and the crack tendency of the sample decreased significantly. Huang [23] studied the effect of LaB_6 addition on grain size and crack elimination of TiAl alloy, and optimized the microstructure, phase transformation texture and mechanical properties at room temperature and high temperature. Wang [24] studied the cracking mechanism of TiAl alloy prepared by SLM (Selective Laser Melting) method, and put forward a new strategy to eliminate cracks. The research revealed that laser remelting results in the material acquiring a refined and uniform grain structure, devoid of cracks and pores, thereby exhibiting enhanced strength and wear resistance [25]. The application of laser surface remelting on H21 steel has been found to effectively reduce both the size and density of cracks [26]. The effect of the layer-by-layer laser remelting process on selected laser-melted 316 L stainless steel samples was investigated by Chen [27]. It was discovered that through controlling the number of remelting times, laser remelting can effectively suppress defects and significantly enhance surface roughness, microhardness, ultimate strength, and strain. Some studies have shown that laser remelting can eliminate cracks and pores in the coating, enhance the adhesion between the coating and the substrate, and improve the hardness and wear resistance [28–31]. Lu [32] prepared the iron-based amorphous coating by three laser scanning methods and obtained the crack-free cladding layer. Laser remelting basically eliminates the coating defects, and greatly improves the elastic modulus and toughness of the coating. The mechanism of selective laser melting, selective electron beam melting and electron beam welding cracks in TiAl alloys has been studied [24, 33, 34]. However, there are few reports on the crack mechanism of TiAl alloy prepared by LDED, and there is no mature theory and method for crack suppression of TiAl alloy. Revealing the crack mechanism is the premise of crack elimination.

In order to solve the problem of cracks in the LDED process of Ti-48Al-2Cr-2Nb alloy, the influence of process parameters on cracks was analyzed. The mechanism of cracks in LDED of Ti-48Al-2Cr-2Nb alloy was analyzed based on microstructure, phase composition, crystal orientation and element composition. The process parameters were optimized by response surface methodology(RSM) to suppress the cracks caused by lack of fusion. By using the optimized parameters, laser remelting was carried out on the sample, which effectively inhibited the crack generation and prepared the crack-free sample. It provides theoretical basis and technical support for LDED manufacturing of light alloy and high temperature titanium alloy, and is of great significance for promoting the engineering application of high-end equipment.

2. Material and experimental procedures

The test employed Ti-48Al-2Cr-2Nb TiAl alloy powder with a particle size ranging from 53 to 150 μm. The chemical composition of the powder is presented in table 1. The substrate material used was Ti-6Al-4V titanium alloy, which had a thickness of 10 mm. Prior to the experiment, the surface of the substrate was meticulously cleaned to remove any oxide film, oil, or other impurities. The experimental setup utilized LDM-4030 powder feeding laser additive manufacturing equipment manufactured by Nanjing Raycham Laser Technology Co.Ltd To prevent oxidation during deposition, argon gas was introduced as a protective atmosphere before testing commenced, ensuring that the oxygen content within the chamber remained below 10ppm. After the completion of deposition, samples were cut using wire electrical-discharge machines. Subsequently, they were embedded and subjected to polishing by immersing in etching liquid (HF: HNO_3: H_2O volume ratio of 1:1:8) for a duration of 5 s. Finally, metallographic samples were prepared following the etching procedure.

Table 1. Composition of Ti-48Al-2Cr-2Nb alloy.

Element	Ti	Al	Cr	Nb	N	O
Content (wt/%)	Bal.	31.50 ~ 33.5	2.3 ~ 3.3	4.3 ~ 5.3	⩽0.02	⩽0.1

Table 2. Process parameter range of LDED of Ti-48Al-2Cr-2Nb Alloy.

	Code		
Parameter	Low(−1)	Medium(0)	High(+1)
Laser power(W)	1000	1400	1800
Travel speed(mm/s)	5	7	9
Powder feed rate(g/min)	4	5.5	7

The microstructure and elemental composition of the metallographic samples were observed and analyzed using an Olympus GX51 optical microscope (OM) and a Hitachi S-3400N scanning electron microscope (SEM). Additionally, EBSD analysis was performed on the samples using a TESCAN MIRA3 field emission scanning electron microscope. Furthermore, phase analysis of the sample was conducted using Cu Kα radiation x-ray diffraction (XRD) with a voltage of 40 kV and current of 30 mA, covering a scanning angle range from 25° to 85°.

The response surface method was employed to design the experimental scheme using the three-factor and three-level Box-Behnken test method. The independent variables were laser power (P), travel speed (V), and powder feed rate (F). Design-Expert software generated multiple sets of process parameters for conducting single-pass single-layer LDED tests with a scanning length of 20 mm. To ensure sample effectiveness, three samples were prepared for each set of process parameters, and the total number of cracks in these samples was calculated. The optimization objective was to minimize the sum of crack numbers. Table 2 presents the range of experimental design parameters.

3. Results and discussion

3.1. Influence of process parameters on cracks

The influence of different laser powers on the crack formation in Ti-48Al-2Cr-2Nb alloy by LDED is illustrated in figure 1. As the laser power increases, the cladding width exhibits a continuous increment. At a laser power level of 1000 W, the sample width reaches its minimum value; however, an abundance of unmelted powder is observed on the surface along with a high occurrence of cracks. The cross-sectional topography reveals extensive presence of unmelted powder and indicates lack of fusion within the sample. When the laser power is 1400 W and 1800 W, the number of cracks is reduced compared with that of 1000 W. With increasing power, the amount of unmelted powder on the surface gradually decreases. Cross-sectional morphology observations indicate that lack of fusion phenomena disappear and the number of cracks decreases, although a few internal cracks still remain. When the laser power reaches 2000W, oxidation occurs on the surface of the sample, and the cladding width reaches the maximum. After examining the sample's surface and cross-section, it is evident that a few cracks still persist, indicating that excessive laser power fails to mitigate crack formation. Moreover, an excessive degree of surface oxidation also detrimentally affects the mechanical properties of the sample.

Figure 2 shows the effect of different travel speed on cracks in Ti-48Al-2Cr-2Nb alloy fabricated by LDED. With the increase of travel speed, the cladding width decreases continuously. The sample with a travel speed of 5.0 mm s^{-1} is the widest, which is due to the reduction of the travel speed, resulting in a high laser energy input in the region, a wider range of molten pool, more powder will fall into the area, it is found through the crack cross section topography that there is lack of fusion at one end of the crack, resulting in a crack. When the travel speed is 7 mm s^{-1}, there is rough texture on the surface of the sample, which indicates that the powder is just completely melted. However, by observing the cross-sectional morphology, a large number of cracks are found in the sample. There are unmelted powders on the surface with the speed of 9 mm s^{-1}, which indicates that the laser with too fast travel speed does not have enough time to melt the powders. By observing the cracks, it is found that the cracks appear due to the lack of fusion on the surface.

Figure 3 shows the macroscopic morphology of cracks in Ti-48Al-2Cr-2Nb alloy by LDED with different powder feed rates. With the increase of powder feed rate, the cladding width has little change. When the powder

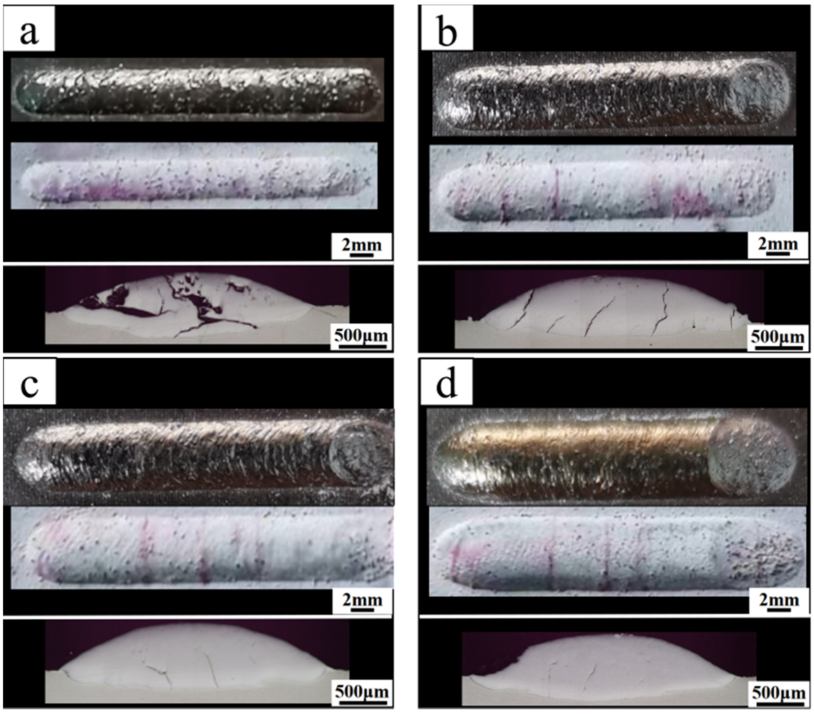

Figure 1. Macroscopic morphology of cracks in Ti-48Al-2Cr-2Nb alloy under different laser powers (Travel speed = 7 mm s^{-1}, Powder feed rate = 5.5 g min^{-1}) (a) 1000 W, (b) 1400 W, (c) 1800W, (d) 2000W.

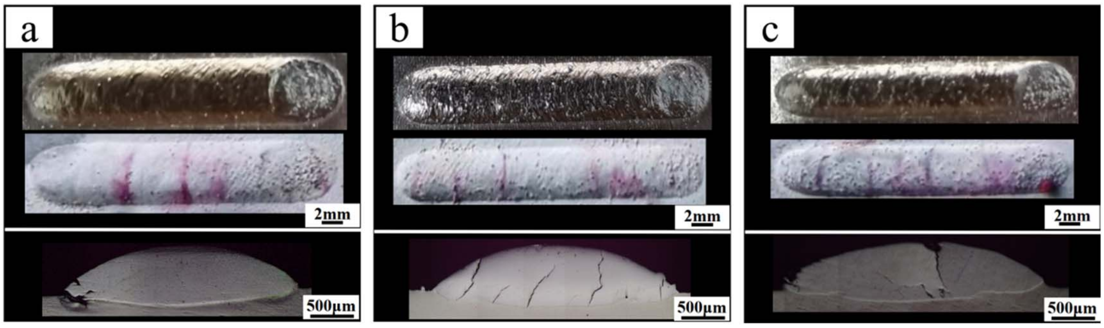

Figure 2. Crack macroscopic and cross-sectional morphology of Ti-48Al-2Cr-2Nb alloy at different travel speed(Laser power = 1400 W,Powder feed rate = 5.5 g min^{-1}) (a)5.0 mm s^{-1}, (b) 7.0 mm s^{-1}, (c) 9.0 mm s^{-1}.

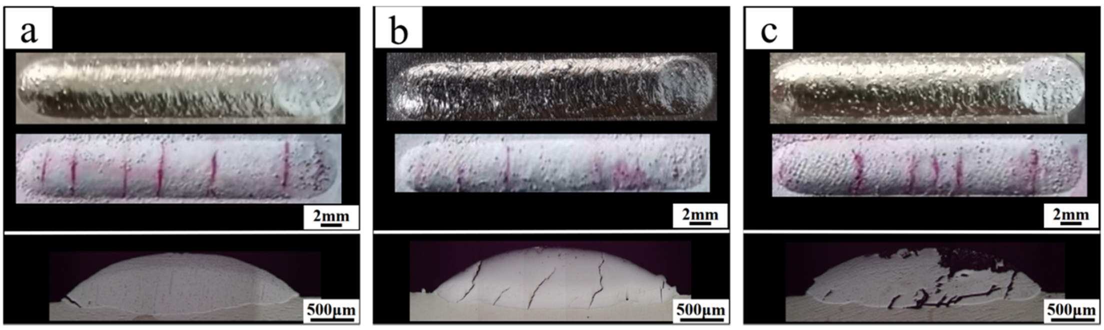

Figure 3. Effect of different powder feed rates on crack macroscopic morphology and cross-sectional morphology of Ti-48Al-2Cr-2Nb alloy (Laser power = 1400 W,Travel speed = 7.0 mm s^{-1}) (a) 4.0 g min^{-1}, (b) 5.5 g min^{-1}, (c) 7.0 g min^{-1}.

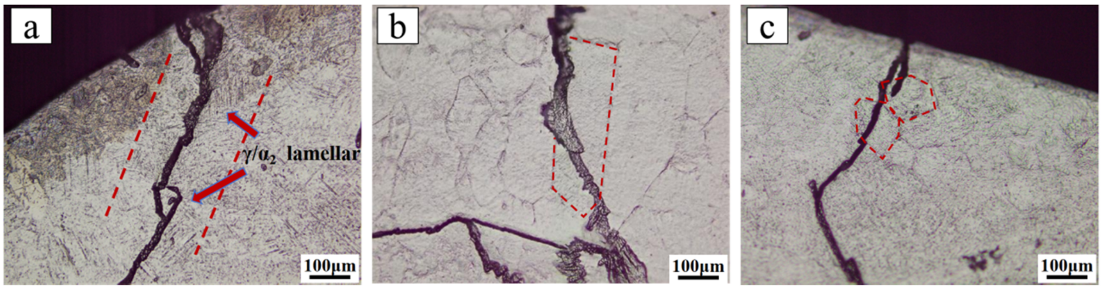

Figure 4. Optical microstructure of crack area by LDED.

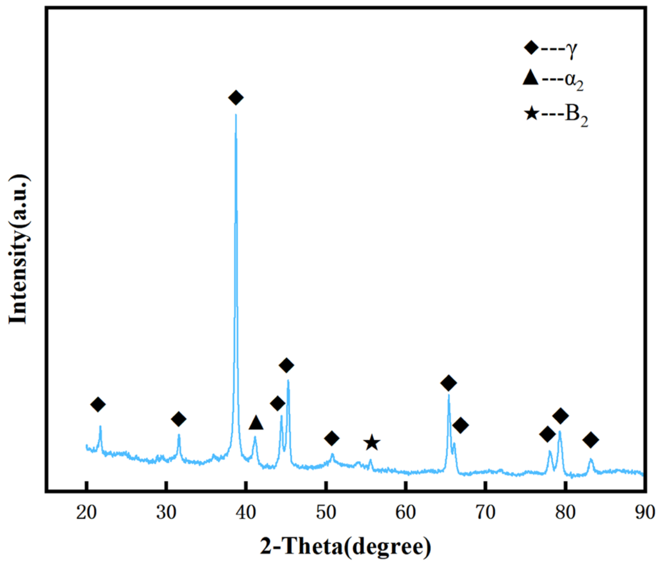

Figure 5. Surface XRD spectrum of crack region of Ti-48Al-2Cr-2Nb alloy sample.

feed rate is 4.0 g min^{-1}, meticulous examination of the cross-sectional morphology reveals an absence of lack of fusion phenomena within the sample; however, cracks persist along the periphery of the cladding layer. When the powder feed rate is 7.0 g min^{-1}, the sample exhibits residual unmelted powder on its surface.According to the cross-sectional morphology, it is observed that a significant number of deep cracks are present in the sample due to lack of fusion.

3.2. Microstructure analysis

Figure 4 shows the microstructure near the crack of Ti-48Al-2Cr-2Nb alloy by LDED. As shown in figure 4(a), it is γ/α_2 lamellar structure near the crack, and its lamellar spacing is small, about 10 μm. It can be seen from figures 4(b) and (c) that the crack mainly occurs in the form of transgranular fracture, and the main reason for the transgranular crack is the increase of residual stress. When the stress exceeds the strength of the material, cracks occur in the poor plasticity TiAl alloy [35].

X-ray (XRD) analysis was carried out on the surface of the sample containing cracks. The result is shown in figure 5. The diffraction peak phase of the sample consists of a large number of γ phase, a small amount of α_2 phase and B_2 phase. The B_2 phase is the ordered structure of the β phase, and the B_2 phase is the body-centered cubic β phase ordered structure at low temperature, which can stably exist in the Al-poor region of γ-TiAl containing refractory metal elements. The diffraction angles of 38.70° and 41.09° are α_2 phase, the diffraction angles of 21.75°, 31.60°, 44.40°, 45.27°, 65.40°, 66.00°, 78.08° and 79.27° are γ phase, and the diffraction angles of B_2 phase are 55.59° and 71.65° respectively.

The crack region was analyzed using EBSD, as depicted in figure 6(a). The phase composition results were found to be consistent with those obtained from XRD, encompassing the presence of α_2, B_2, and γ phases. Notably, the α_2 phase accounted for 3.10% while the B_2 phase accounted for 3.28%. In the crack-free region, the phase composition is mainly γ phase, and a small amount of B_2 phase exists. In the area near the crack, α_2 phase

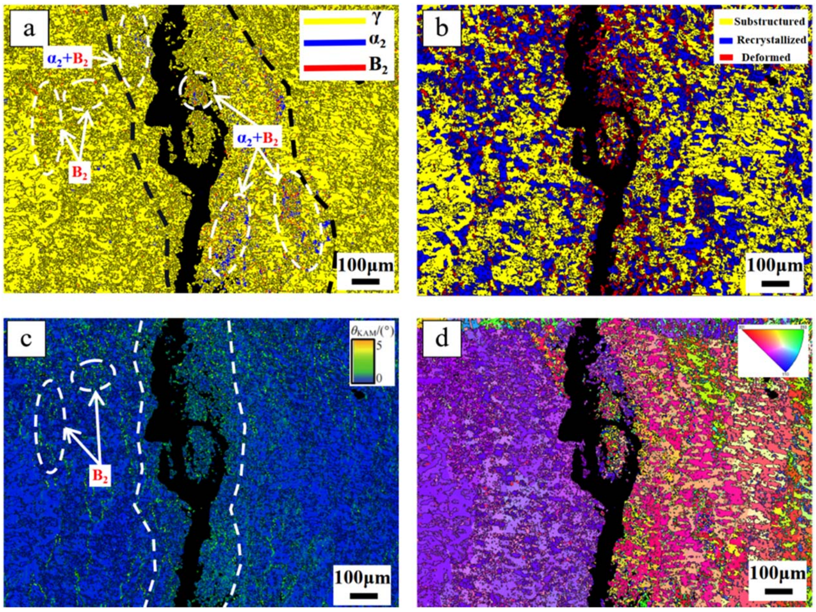

Figure 6. EBSD analysis of samples with cracks. (a) phase distribution, (b) recrystallization distribution, (c) local orientation difference, (d) crystal orientation.

and B_2 phase congregate, and B_2 phase exists around α_2 phase, which indicates that the crack is easy to form in the area where α_2 phase and B_2 phase congregate. Because α_2 phase has a very limited slip system ⟨112(—)1⟩ {0001}, the activation of the slip system requires great shear stress, which leads to the brittle phase characteristic of α_2 [36]. At room temperature, the thermal expansion coefficients of α_2 phase and B_2 phase are $3.26 \times 10^{-5}K^{-1}$ and $1.45 \times 10^{-5}K^{-1}$, respectively. Because the thermal expansion coefficients of B_2 phase change more sharply with temperature, the difference of thermal expansion coefficients increases with temperature [30, 37]. In the LDED process, the difference of thermal expansion coefficient will increase with higher temperature, which will eventually lead to greater stress between the two phases.

The B_2 phase is also present in the crack-free zone, and it exhibits brittleness and hardness. However, cracks do not occur within the region solely composed of the B_2 phase. This phenomenon can be attributed to the beneficial effect of a certain amount of B_2 phase on enhancing the plasticity of TiAl alloy, as well as its ability to impede pore and crack growth at elevated temperatures, thereby improving material's plastic deformation capability [38, 39]. The presence of the B_2 phase also contributes to the enhancement of superplastic deformation in TiAl-based alloys [40–42]. The occurrence of cracks is more likely in the aggregation region of α_2 phase and B_2 phase, indicating that the stress in the B_2 phase is comparatively lower than that in both α_2 and B_2 phases. As depicted in figure 6(c), there are some stresses present in the region where the B_2 phase is located without any cracks; however, the stress concentration is lower compared to that observed in the gathering region of α_2 and B_2 phases.

The distribution of recrystallization near the crack is depicted in figure 6(b), where deformed grains are predominantly concentrated. This concentration arises from plastic deformation, resulting in a high defect density within the crystal and an evident gradient in grain orientation distribution. The recrystallization distribution of the sample is illustrated in figure 6(b). It can be observed from the figure that Deformed grains are predominantly concentrated near the crack due to their formation through plastic deformation, resulting in a higher defect density within the crystal and an evident gradient in grain orientation distribution. The volumetric proportion of substructured grains amounts to 46.3%. In comparison with deformed grains, the substructured grains undergo a recovery process, resulting in reduced defect density and orientation dispersion. The analysis of figure 6(b) reveals that the deformed grains are primarily localized in close proximity to the crack. Recrystallized grains constitute 40.1% of the volume fraction during LDED, as higher temperature gradients induce partial dynamic recrystallization in TiAl alloy by storing deformation energy as its driving force. Following dynamic recrystallization, dislocations within deformed grains are released; hence, dynamic recrystallized microstructure experiences lower stress compared to its deformed counterpart while greater stress persists in the microstructure adjacent to the crack due to unreleased dislocation accumulation.

The KAM layout of the sample is depicted in figure 6(c), revealing that the local orientation difference near the crack exhibits maximum values. This observation suggests a high dislocation density in this region, indicating significant stress concentration adjacent to the crack. As depicted in figure 6(a), the region exhibiting

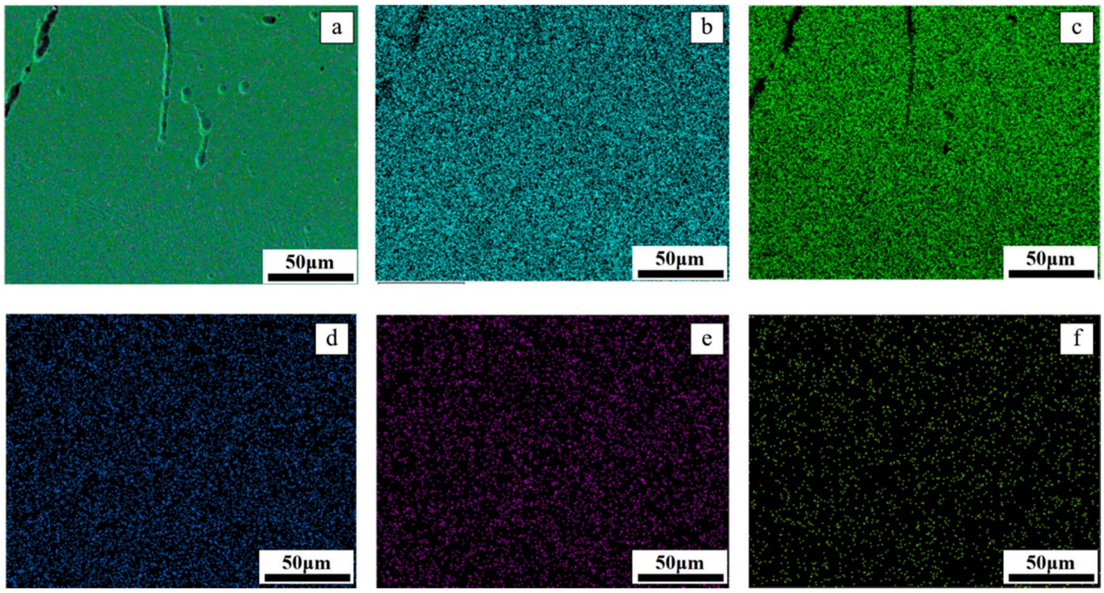

Figure 7. EDS analysis on the surface of samples with cracks. (a): Overall distribution map, (b):Ti, (c):Al, (d):V, (e):Nb, (f):Cr.

significant local orientation difference is primarily located within the aggregation zone of α_2 and B_2 phases. Due to dissimilar thermal expansion coefficients between these two phases, which further increase at higher temperatures, a substantial amount of heat is generated during LDED process leading to elevated stress levels at their interface.

The crystal orientation difference between the γ phase on both sides of the crack is evident in figure 6(d). Analysis of figures 6(b) and (c) reveals that this disparity arises from the continuous generation of brittle phases α_2 and B_2, as well as the accumulation of residual stress during LDED. In areas where a significant number of dislocations and unreleased stresses exist, such as the crack formation region, crystal orientation undergoes changes leading to substantial differences in regional structure.

In order to investigate the influence of element distribution on crack formation, the element content near the crack was detected. Figure 7 illustrates the distribution of elements in the cracked sample. It is evident that there is a decrease in titanium (Ti) content at deeper locations within the crack. Additionally, aluminum (Al) exhibits significant loss near the crack site. Notably, when compared to titanium and niobium (Nb), aluminum experiences substantial vaporization due to its high saturated vapor pressure under conditions of intense energy input [43]. V, Nb and Cr are uniformly distributed.

3.3. Crack formation mechanism and suppression method of Ti-48Al-2Cr-2Nb alloy via LDED

Figure 8 is a schematic diagram of crack generation mechanism of TlAl alloy manufactured by LDED. From the analysis of figures 1–3, it can be seen that lack of fusion is caused by unreasonable matching of process parameters, which leads to incomplete melting of powder. Lack of fusion exists on the surface and inside of the sample. Due to the inclusion of a large number of pores and unmelted powder in the lack of fusion area, cracks are easy to occur in the lack of fusion area under the action of residual stress generated during LDED, and the cracks generated in this area are all large-size cracks, which have a great negative impact on mechanical properties. In order to restrain the crack caused by lack of fusion, the method of optimizing process parameters is generally adopted, and the heat input is optimized by adjusting laser power, travel speed and powder feed rate to restrain the crack caused by lack of fusion.

The driving force of laser directed energy deposited TiAl alloy crack is composed of two kinds of stresses, one is the stress between different phases. Because the thermal expansion coefficients of α_2 phase and B_2 phase are different, and the difference of thermal expansion coefficients will increase continuously at higher temperature, which eventually leads to greater stress between the two phases. The other is residual stress. During LDED, the powder melts in the molten pool. With the movement of laser, the heat will diffuse to the substrate with the fastest heat dissipation, and the molten metal will solidify rapidly. Because of the different composition of cladding layer and substrate, the solidification shrinkage is different, resulting in residual stress. Under the action of stress, transgranular fracture occurs preferentially in the region where α_2 phase and B_2 phase gather. At the same time, due to the high saturated vapor pressure of Al, Al is more volatile than other elements. During the LDED process, Al is volatilized due to high temperature. The decrease of Al content will shift the solid–liquid

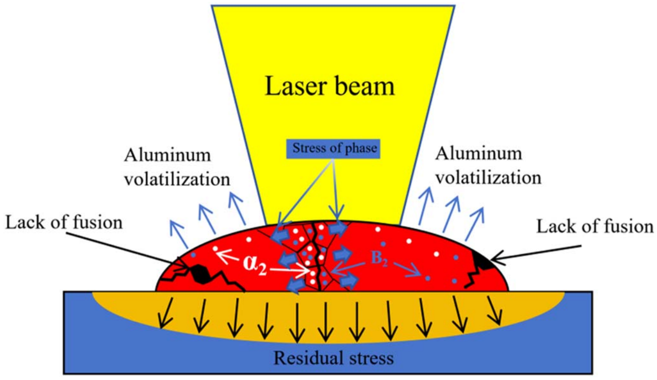

Figure 8. Schematic diagram of crack generation mechanism of Ti-48Al-2Cr-2Nb alloy manufactured by LDED.

Table 3. Designed experiment and results.

Run	Laser power (W)	Travel speed (mm/s)	Powder feed rate (g/min)	Number of cracks Group 1	Group 2	Group 3	Sum of the number of cracks
1	1400	7	5.5	5	6	6	17
2	1800	7	4	2	3	1	6
3	1400	5	4	7	6	7	20
4	1400	7	5.5	8	6	7	21
5	1400	7	5.5	6	5	7	18
6	1000	9	5.5	11	9	12	30
7	1400	7	5.5	5	4	6	15
8	1800	7	7	1	2	0	3
9	1800	5	5.5	5	4	4	13
10	1800	9	5.5	4	5	3	12
11	1400	9	7	6	4	6	16
12	1000	7	7	10	12	8	30
13	1400	7	5.5	7	6	5	19
14	1000	7	4	6	8	7	21
15	1000	5	5.5	10	8	6	24
16	1400	9	4	4	4	3	11
17	1400	5	7	5	3	6	14
18	1400	7	5.5	4	6	5	15

phase line of TiAl alloy phase diagram to the direction of aluminum depletion, which will promote the precipitation of brittle phase α_2, lead to the increase of aggregation area of α_2 and B_2, and promote the generation of cracks. In order to reduce the stress generated during LDED of TiAl alloy, the main methods are to increase the thermal energy input, prolong the cooling time and reduce the temperature gradient.

3.4. Effect of optimization of process parameters on crack suppression

The number of cracks in three samples prepared under different combinations of process parameters for Ti-48Al-2Cr-2Nb alloy, optimized using the RSM method for LDED process, is presented in table 3. It can be observed that all samples fabricated with varying process parameters exhibited cracks, ranging from a minimum of 1 to a maximum of 12. This clearly indicates the significant influence of process parameters on crack formation, and the occurrence of cracking sound during post-cladding cooling.

The experimental results in table 3 were fitted with the software Design-Expert, and the mathematical regression model of the number of cracks was constructed. The statistical data of crack number were analyzed and tested by ANOVA. The specific results are shown in table 4. The results of variance analysis show that laser power is the main factor affecting cracks. The F value of the model is 13.71, which shows that the model is significant. Significance test value P value is 0.006, less than 0.05; Lack of fit is 0.0076; The correlation coefficient R_2 is 0.9391, which is close to 1, and the adjusted R_2 is 0.8706, and the difference is less than 0.2, which indicates that the model has good correlation; The signal-to-noise ratio (Adequate Precision) is 14.0493, which is greater than 4, which indicates that the model has a good fitting degree and can obtain a more accurate mathematical

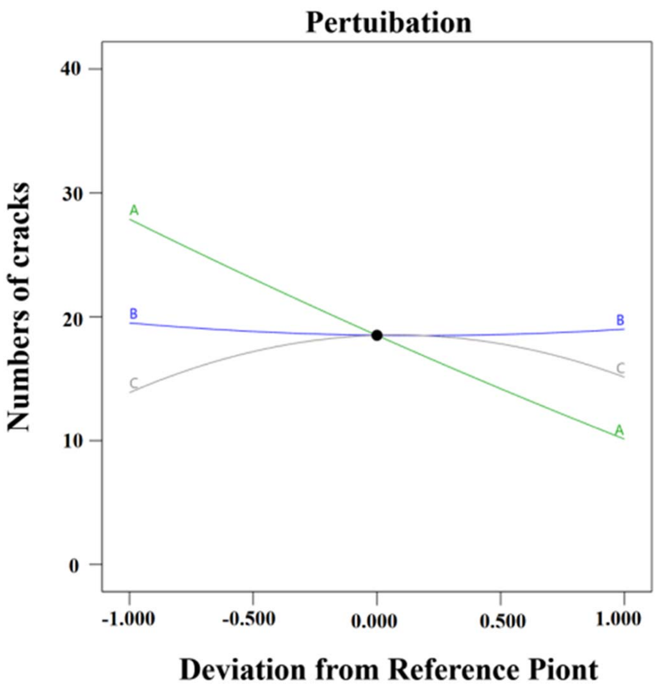

Figure 9. Perturbation plots showing the influences of the laser process parameters on numbers of cracks.

Table 4. Analysis of variance for the numbers of cracks.

Source	Sum of squares	Degree of freedom	Mean square	F-value	P-value
Model	782.86	9	86.98	13.71	0.0006
A-Laser power	630.13	1	630.13	99.33	<0.0001
B-Travel speed	0.5000	1	0.5000	0.0788	0.7860
C-Powder-feed rate	3.13	1	3.13	0.4926	0.5027
AB	12.25	1	12.25	1.93	0.2021
AC	36.00	1	36.00	5.67	0.0444
BC	30.25	1	30.25	4.77	0.0605
A^2	1.09	1	1.09	0.1720	0.6893
B^2	2.45	1	2.45	0.3869	0.5512
C^2	69.82	1	69.82	11.01	0.0106
Residual	50.75	8	6.34		
Lack of Fit	45.25	3	15.08	13.71	0.0076
Pure Error	5.50	5	1.10		
Cor Total	833.61	17			

model of crack number [44, 45]. Therefore, the response regression prediction model of crack number was derived as shown in equation (1):

$$Y = 18.5 - 8.87A - 0.25B + 0.625C - 1.75AB \\ -3AC + 2.75BC + 0.5A^2 + 0.75B^2 - 4C^2 \quad (1)$$

3.4.1. Effect of process parameters on the number of cracks

Figure 9 is a perturbation diagram of the influence of the Design-Expert software on the LDED manufacturing process parameters and the number of cracks based on the data in table 2. It can be seen from the curve in the figure that the influence of laser power (A) on cracks is the most significant, and the number of cracks decreases gradually with the increase of laser power (A) within the selected parameter range; Scanning velocity has little effect on cracks. With the increase of scanning velocity (B), the number of cracks decreases slightly at first and then increases slightly; For the powder feed rate (C), with the increase of the powder feed rate, the number of cracks increases, and when the increase exceeds the critical value, the number of cracks decreases.

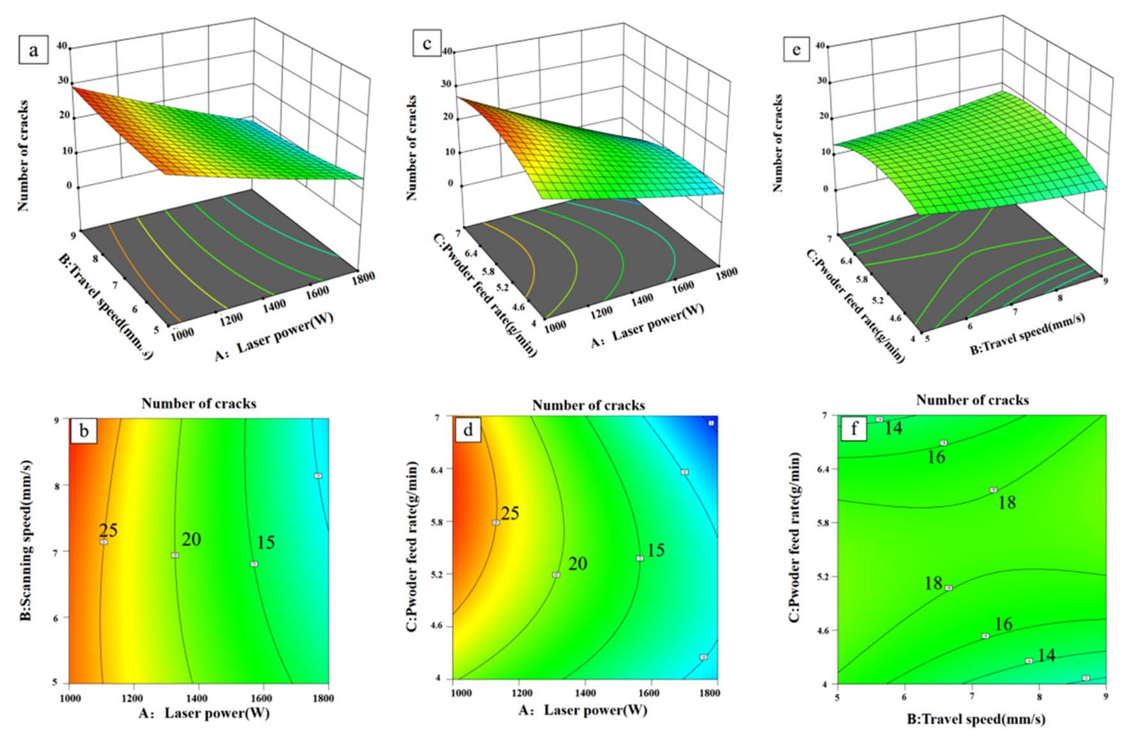

Figure 10. 3D response surface map and contour plot of interaction effects on numbers of cracks. (a), (b) Laser power and Travel speed; (c), (d) Laser power and Powder feed rate; (e), (f) Travel speed and Powder feed rate.

Figures 10(a) and (b) depict the response surface diagram and contour diagram of laser power and travel speed relative to the number of cracks. An increase in laser power results in a gradual reduction of the number of cracks [46]. The findings indicate that augmenting heat input facilitates the mitigation of crack generation. This is primarily attributed to the increased energy input into the molten pool under high laser power conditions, resulting in a diminished temperature gradient and reduced residual stress [47, 48]. Consequently, the number of cracks is diminished. As the travel speed escalates, the number of cracks initially amplifies and subsequently diminishes. The contour diagram reveals that a reduction in the number of cracks is achieved when the travel speed is 7 mm s^{-1} and the laser power ranges from 1000 W to 1800W, resulting in a decrement from 25 to 15 cracks.

The figures 10(c) and (d) depict the response surface diagram and contour diagram of laser power and response surface diagram as influenced by the number of cracks. A gradual decrease in the number of cracks is observed with the increment of laser power. The increment in powder feed rate initially leads to a reduction in the number of cracks, followed by an increase in their count. The minimization of powder feed rate is attributed to the limited amount of powder that can be melted in the molten pool. An increase in powder feed rate enables more powder to be melted, thereby enhancing energy input [19]. This leads to a reduction in the number of cracks. As the powder feed rate continues to escalate, an excessive amount of powder may not be completely melted in the melt pool. Consequently, a portion of the energy is diverted by the surplus splashing powder, leading to lack of fusion. This, in turn, indirectly diminishes the energy input of the laser, resulting in an increased propensity for cracks. The powder feed rate of 5.5 g min^{-1} and the laser power ranging from 1000 W to 1800W were observed to decrease the number of cracks from 25 to 15, as evident from the contour diagram.

The response surface diagram and contour diagram in figures 10(e) and (f) illustrate the influence of travel speed and powder feed rate on crack formation. According to the contour diagram, the number of cracks in the sample, prepared by matching parameters of varying scanning speed and powder delivery rate, ranged between 14 and 18, exhibiting a hyperbolic influence trend.The amount of powder falling into the molten pool is primarily determined by the powder feed rate and travel speed. When the ratio of these two rates remains constant, the quantity of powder entering the pool during a specific time interval remains fixed. Under consistent laser power conditions, minor variations in laser energy input and temperature gradient result in a negligible impact on the number of cracks, regardless of changes in the scanning speed and powder feed rate.

3.4.2. Optimization of process parameters based on RSM

The RSM algorithm was used to optimize the regression prediction model of crack and process parameters (laser power, travel speed and powder feed rate). Formula (2) is introduced [49], where N is the number of response

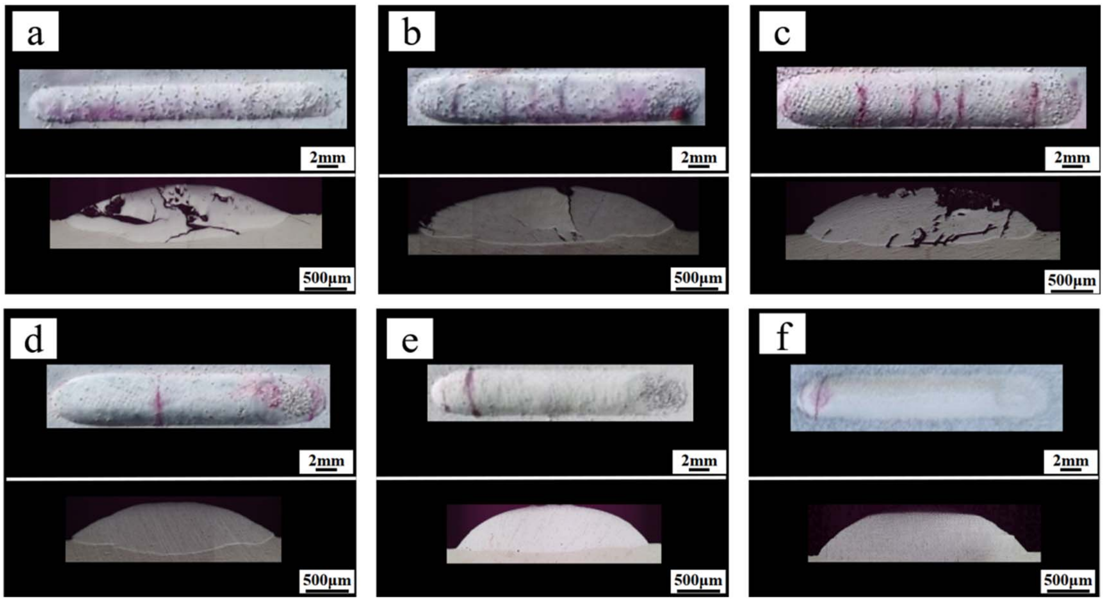

Figure 11. The surface and cross section morphology of the sample before and after the optimization of the process parameters. Unoptimized : (a) 1000 W, 7.0 mm s^{-1}, 5.5 g min^{-1}; (b) 1400 W, 9.0 mm s^{-1}, 5.5 g min^{-1}; (c) 1400 W, 7.0 mm s^{-1}, 7.0 g min^{-1}; Optimized: (d) ~ (f) 1800W, 6.0 mm s^{-1}, 7.0 g min^{-1}.

values, r_i is the importance of a specific response surface, and d_i represents the local satisfaction function of some specific response values.

$$Desirablity = \left[\prod_{i=1}^{N} d_i^{r_i}\right]^{\frac{1}{\sum r_i}} \tag{2}$$

In order to minimize the number of cracks produced by laser adding materials, the response target value of crack number was selected as the minimum in the range of 3–30, and the importance was 5+. The optimized laser parameters were: laser power 1800W, travel speed 6.0 mm s^{-1}, powder feed rate 7 g min^{-1}. Under these parameters, the predicted number of cracks was 3.563 and desirability was 0.979.

The macroscopic morphologies of the three groups of samples prepared before optimizing the process parameters are shown in figures 11(a)–(c). The unoptimized process parameters result in lack of fusion and an increased presence of unmelted powder and cracks on the surface. In contrast, figures 11(d)–(f) display the macroscopic morphologies of the three groups of samples prepared with optimized parameters. Compared to figures 11(a)–(c), there is a significant reduction in both unmelted powders and surface cracks observed after parameter optimization. Although lack of fusion is eliminated through parameter optimization, some cracks still remain present on the sample's surface. This indicates that while optimizing process parameters effectively reduces cracks caused by lack of fusion, it cannot completely eliminate those resulting from stress between different phases during additive manufacturing.

Figures 11(a)–(c) show the macroscopic morphology of cracks in three groups of samples prepared before the optimization of process parameters. It can be found that the unoptimized process parameters have lack of fusion, and there are more unmelted powders and more cracks on the surface. Figures 8(d)–(f) show the macroscopic morphology of cracks in the three groups of samples prepared with optimized parameters. Compared with figures 11(a)–(c), the number of unmelted powders and cracks on the surface is obviously reduced. Through the observation of cross-sectional morphology, no lack of fusion is found, and a good metallurgical bond is formed between the cladding layer and the substrate. From the macroscopic morphology of the sample, it can be seen that the sample after parameter optimization eliminates the lack of fusion phenomenon and still has cracks, which shows that the optimization of process parameters can effectively reduce the cracks caused by lack of fusion, but can not completely eliminate the cracks caused by the stress between different phases in the process of LDED.

3.5. Effect of laser remelting on crack suppression

After the completion of LDED on the sample, powder feed is halted, and a laser with equivalent excitation power is employed to perform surface rescanning for achieving *in situ* laser remelting during the deposition process. The surface and cross-sectional morphologies of samples without remelting, remelted once, and remelted 5

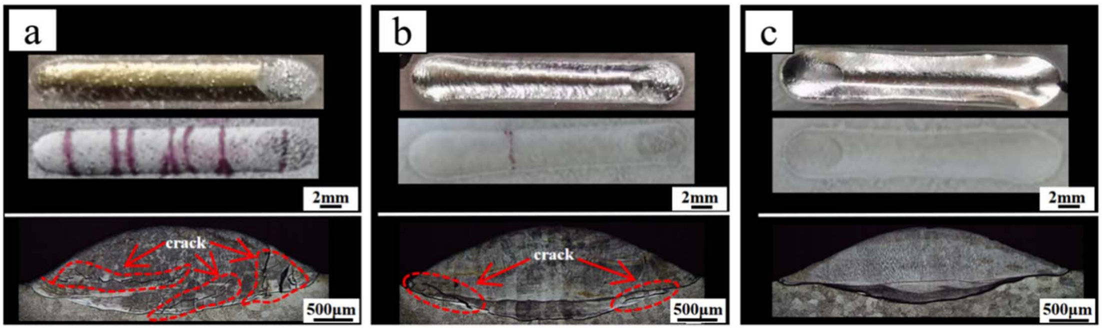

Figure 12. Effect of laser remelting on crack suppression. (a) Without remelting; (b) Remelted once; (c) Remelted 5 times.

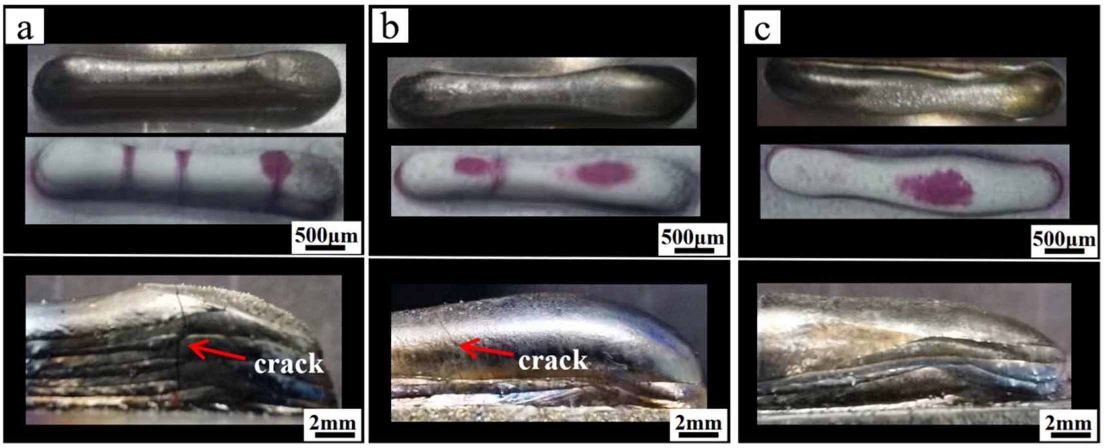

Figure 13. Influence of laser remelting times on samples deposited with 10 layers (a) Without remelting; (b) Remelted once; (c) Remelted 2 times.

times are shown in figure 12 respectively. As the number of laser remelting times increased, a decreasing trend in crack formation was observed along with a reduction in the presence of adhering powder on the sample surface. A crack-free sample was achieved after 5 remelting times. The macroscopic morphology of the surface and side of the sample with 10 layers of LDED is depicted in figure 13. It can be observed from the figure that the sample devoid of remelting exhibits a prominent crack, extending from the substrate to the uppermost region. After one remelting, the degree of cracking decreased compared to that observed without undergoing any remelting process. After two subsequent remelting, the occurrence of cracks in the sample was completely eradicated. The results demonstrate the effective crack inhibition achieved through laser remelting, as this process enhances energy input, reduces cooling rates to a certain extent, reduces temperature gradients, alleviates residual stress, and effectively suppresses crack formation. For the sample exhibiting lack of fusion on its surface, remelting can effectively address this issue by eliminating cracks resulting from lack of fusion and facilitating crack suppression.

4. Conclusion

The present study investigates the influence of various process parameters on crack formation in Ti-48Al-2Cr-2Nb alloy by LDED. The underlying mechanism responsible for crack initiation is elucidated. To suppress cracks resulting from lack of fusion, the RSM is employed to optimize the process parameters, leading to successful crack-free fabrication of samples through laser remelting. In summary, this paper provides a comprehensive analysis as follows:

1. The crack of the Ti-48Al-2Cr-2Nb alloy by LDED exhibits a layered structure consisting of γ/α_2 lamellar structure, with transgranular fracture being the predominant mode of failure. The LDED phases in the sample primarily comprise α_2, B_2, and γ phases. In close proximity to the crack, there is observed aggregation of α_2 and B_2 phases.

2. The elevated temperature induces the volatilization of aluminum, thereby facilitating the formation of the brittle α_2 phase and subsequently promoting the formation of agglomeration area of α_2 and B_2 phase.

3. The influence of laser power on crack formation is highly significant, as an increase in laser power leads to a gradual reduction in the number of cracks. Optimization of process parameters can effectively mitigate the cracks caused by lack of fusion; however, cracks caused by stress between different phases cannot be eliminated.

4. Laser remelting following LDED exhibits characteristics such as reduced temperature gradient, cooling rate and residual stress. This process effectively inhibits the formation of cracks in Ti-48Al-2Cr-2Nb alloy during LDED.

Acknowledgments

The authors would like to acknowledge the financial supports provided by the National Key Research and Development Program of China (2022YFB4602202) and Liaoning BaiQianWan Talents Program (LNBQW 2020B0050).

Data availability statement

All data that support the findings of this study are included within the article (and any supplementary files).

ORCID iDs

Baolei Cui https://orcid.org/0009-0006-7243-2285

References

[1] Xu R, Liang N, Zhuang L, Wei D and Zhao Y 2022 Microstructure and mechanical behaviors of Al/Cu laminated composites fabricated by accumulative roll bonding and intermediate annealing *Mater. Sci. Eng.* A **832** 142510
[2] Bewlay B P, Weimer M, Kelly T, Suzuki A and Subramanian P R 2013 The science, technology, and implementation of TiAl alloys in commercial aircraft engines *MRS Online Proceedings Library (OPL)* **1516** 49–58
[3] Bewlay B P, Nag S, Suzuki A and Weimer M J 2016 TiAl alloys in commercial aircraft engines *Mater. High Temp.* **33** 549–59
[4] Lu B, Li D and Tian X 2015 Development trends in additive manufacturing and 3D printing *Engineering* **1** 085–9
[5] Brandt M 2016 *Laser Additive Manufacturing- Materials, Design, Technologies, and Applications* (Woodhead Publishing)
[6] Gong G, Ye J, Chi Y, Zhao Z, Wang Z, Xia G and Chen C 2021 Research status of laser additive manufacturing for metal: a review *Journal of Materials Research and Technology* **15** 855–84
[7] Li N, Huang S, Zhang G, Qin R, Liu W, Xiong H and Blackburn J 2019 Progress in additive manufacturing on new materials: a review *J. Mater. Sci. Technol.* **35** 242–69
[8] Wang Y D, Tang H B, Fang Y L and Wang H M 2010 Microstructure and mechanical properties of laser melting deposited 1Cr12Ni2WMoVNb steel *Mater. Sci. Eng.* A **527** 4804–9
[9] Qu H P, Li P, Zhang S Q, Li A and Wang H M 2010 Microstructure and mechanical property of laser melting deposition (lmd) ti/tial structural gradient material *Mater. Des.* **31** 574–82
[10] Yan L, Chen X, Zhang Y, Newkirk J W and Liou F 2017 Fabrication of functionally graded ti and γ-tial by laser metal deposition *JOM* **69** 2756–61
[11] Liu Z, Ma R, Xu G, Wang W and Liu J 2020 Laser additive manufacturing of bimetallic structure from Ti-6Al-4V to Ti-48Al-2Cr-2Nb via vanadium interlayer *Mater. Lett.* **263** 127210
[12] Wu Y, Cheng X, Zhang S, Liu D and Wang H 2019 Microstructure and phase evolution in γ-TiAl/Ti_2AlNb dual alloy fabricated by direct metal deposition *Intermetallics* **106** 26–35
[13] Chen Y, Zhang K, Huang J, Hosseini S R E and Li Z 2016 Characterization of heat affected zone liquation cracking in laser additive manufacturing of inconel 718 *Materials & Design* **90** 586–94
[14] Mehta A, Zhou L, Huynh T, Park S, Hyer H, Song S and Sohn Y 2021 Additive manufacturing and mechanical properties of the dense and crack free Zr-modified aluminum alloy 6061 fabricated by the laser-powder bed fusion *Additive Manufacturing* **41** 101966
[15] Uddin S Z, Murr L E, Terrazas C A, Morton P, Roberson D A and Wicker R B 2018 Processing and characterization of crack-free aluminum 6061 using high-temperature heating in laser powder bed fusion additive manufacturing *Additive Manufacturing* **22** 405–15
[16] Soliman H A and Elbestawi M 2022 Titanium aluminides processing by additive manufacturing–a review *Int. J. Adv. Manuf. Technol.* **119** 5583–614
[17] Gussone J, Hagedorn Y C, Gherekhloo H, Kasperovich G, Merzouk T and Hausmann J 2015 Microstructure of γ-titanium aluminide processed by selective laser melting at elevated temperatures *Intermetallics* **66** 133–40
[18] Xu R, Li M and Zhao Y 2023 A review of microstructure control and mechanical performance optimization of γ-TiAl alloys *J. Alloys Compd.* **932** 167611
[19] Liu W and Dupont J N 2004 Fabrication of carbide-particle-reinforced titanium aluminide-matrix composites by laser-eng-ineered net shaping *Metall. Mater. Trans.* A **35** 1133–40
[20] Osakada K and Shiomi M 2006 Flexible manufacturing of metallic products by selective laser melting of powder *Int. J. Mach. Tools Manuf* **46** 1188–93

[21] Sharman A R C, Hughes J I and Ridgway K 2018 Characterisation of titanium aluminide components manufactured by laser metal deposition *Intermetallics* **93** 89–92
[22] Thomas M, Malot T and Aubry P 2017 Laser metal deposition of the intermetallic TiAl alloy *Metall. Mater. Trans.*A **48** 3143–58
[23] Huang D, Zhou Y, Yao X, Tan Q, Chang H, Wang D and Zhang M X 2022 From crack-prone to crack-free: unravelling the roles of LaB6 in a β-solidifying TiAl alloy fabricated with laser additive manufacturing *Mater. Sci. Eng.*A **861** 144358
[24] Wang M S, Liu E W, Du Y L, Liu T T and Liao W H 2021 Cracking mechanism and a novel strategy to eliminate cracks in TiAl alloy additively manufactured by selective laser melting *Scr. Mater.* **204** 114151
[25] Yu Y, Zhang M, Guan Y, Wu P, Chong X, Li Y and Tan Z 2019 The effects of laser remelting on the microstructure and performance of bainitic steel *Metals* **9** 912
[26] Zhang Z, Lin P, Zhou H and Ren L 2013 Microstructure, hardness, and thermal fatigue behavior of H21 steel processed by laser surface remelting *Appl. Surf. Sci.* **276** 62–7
[27] Chen X, Wen K, Mu W, Zhang Y, Huang S and Liu W 2023 Effect of layer-by-layer laser remelting process on the microstructure and performance of selective laser melting 316L stainless steel *Int. J. Adv. Manuf. Technol.* **128** 2221–36
[28] Yang Y, Li J, Yao F and Li X 2023 Effect of laser remelting on the organization and properties of WC/Ni-based coatings generated *in situ* by laser cladding *J. Manuf. Processes* **102** 501–12
[29] Zhou J, Han X, Li H, Liu S and Yi J 2021 Investigation of layer-by-layer laser remelting to improve surface quality, microstructure, and mechanical properties of laser powder bed fused AlSi10Mg alloy *Mater. Des.* **210** 110092
[30] Dos Santos Paes L E, Pereira M, Xavier F A, Weingaertner W L and Vilarinho L O 2022 Lack of fusion mitigation in directed energy deposition with laser (DED-L) additive manufacturing through laser remelting *J. Manuf. Processes* **73** 67–77
[31] Boschetto A, Bottini L and Pilone D 2021 Effect of laser remelting on surface roughness and microstructure of AlSi10Mg selective laser melting manufactured parts *Int. J. Adv. Manuf. Technol.* **113** 2739–59
[32] Lu Y, Huang G, Wang Y, Li H, Qin Z and Lu X 2018 Crack-free Fe-based amorphous coating synthesized by laser cladding *Mater. Lett.* **210** 46–50
[33] Gao R, Peng H, Guo H and Chen B 2021 An innovative way to fabricate γ-TiAl blades and their failure mechanisms under thermal shock *Scr. Mater.* **203** 114092
[34] Chen G, Zhang G, Yin Q and Zhang B 2020 Investigation of cracks during electron beam welding of γ-TiAl based alloy *J. Mater. Process. Technol.* **283** 116727
[35] Shi X, Wang H, Feng W, Zhang Y, Ma S and Wei J 2020 The crack and pore formation mechanism of Ti–47Al–2Cr–2Nb alloy fabricated by selective laser melting *Int. J. Refract. Met. Hard Mater* **91** 105247
[36] Court S A, Löfvander J P A, Loretto M H and Fraser H L 1990 The influence of temperature and alloying additions on the mechanisms of plastic deformation of Ti_3Al *Philos. Mag.* A **61** 109–39
[37] FrÈour S, Gloaguen D, François M and GuillÈn R 2006 Application of inverse models and XRD analysis to the determination of Ti-17 β-phase coefficients of thermal expansion *Scr. Mater.* **54** 1475–8
[38] Imaev V M, Imaev R M, Oleneva T I and Khismatullin T G 2008 Microstructure and mechanical properties of the intermetallic alloy Ti-45Al-6 (Nb, Mo)−0.2 B *The Physics of Metals and Metallography* **106** 641–8
[39] Imayev V, Khismatullin T and Imayev R 2010 Microstructure and technological plasticity of cast intermetallic alloys on the basis of γ-TiAl. The *Phys. Met. Metall.* **109** 402–10
[40] Vanderschueren D, Nobuki M and Nakamura M 1993 Superplasticity in a vanadium alloyed gamma plus beta phased TiAl intermetallic *Scr. Metall. Mater.* **28** 605–10
[41] Nieh T G, Hsiung L M and Wadsworth J 1999 Superplastic behavior of a powder metallurgy TiAl alloy with a metastable microstructure *Intermetallics* **7** 163–70
[42] Masahashi N, Mizuhara Y, Matsuo M, Hanamura T, Kimura M and Hashimoto K 1991 High temperature deformation behavior of titanium-aluminide based gamma plus beta microduplex alloy *ISIJ Int.* **31** 728–37
[43] Kan W, Chen B, Jin C, Peng H and Lin J 2018 Microstructure and mechanical properties of a high Nb-TiAl alloy fabricated by electron beam melting *Mater. Des.* **160** 611–23
[44] Ma M, Xiong W, Lian Y, Han D, Zhao C and Zhang J 2020 Modeling and optimization for laser cladding via multi-objective quantum-behaved particle swarm optimization algorithm *Surf. Coat. Technol.* **381** 125129
[45] Lu P Z, Jia L, Zhang C, Heng X, Xi X C, Duan M F and Zhou Y X 2023 Optimization on laser cladding parameters for preparing Ni60 coating along with its friction and wear properties *Materials Today Communications* **37** 107162
[46] Fu F, Zhang Y, Chang G and Dai J 2016 Analysis on the physical mechanism of laser cladding crack and its influence factors *Optik* **127** 200–2
[47] Cheng M, Zou X, Pan Y, Zhou Y, Liu W and Song L 2023 Residual stress control using process optimization in directed energy deposition *Materials* **16** 6610
[48] Gao Z, Wang L, Wang Y, Lyu F and Zhan X 2022 Crack defects and formation mechanism of FeCoCrNi high entropy alloy coating on TC4 titanium alloy prepared by laser cladding *J. Alloys Compd.* **903** 163905
[49] Sun Y and Hao M 2012 Statistical analysis and optimization of process parameters in Ti6Al4V laser cladding using Nd:YAG laser *Opt. Lasers Eng.* **50** 985–95